PHYSICAL REVIEW B **70**, 035104 (2004)

Temperature-dependent effective mass renormalization in a Coulomb Fermi liquid

Ying Zhang and S. Das Sarma
Condensed Matter Theory Center, Department of Physics, University of Maryland, College Park, Maryland 20742-4111, USA

(Received 2 January 2004; published 14 July 2004)

We calculate numerically the quasiparticle effective mass (m^*) renormalization as a function of temperature and electron density in two- and three-dimensional electron systems with long-range Coulomb interaction. In two dimensions, the leading temperature correction is linear and positive, with the slope being a universal density independent number in the high-density limit. We predict an enhancement of the effective mass at low temperatures and a nonmonotonic temperature dependence at higher temperatures ($T/T_F \sim 0.1$) with the peak shifting toward higher temperatures as density decreases. In three dimensions, we find that the effective mass temperature dependence is nonlinear and nonuniversal, and depends on the electron density in a complicated way. At very high densities, the leading correction is positive, while at lower densities, it changes sign and the effective mass decreases monotonically from its zero-temperature value with increasing temperature.

DOI: 10.1103/PhysRevB.70.035104 PACS number(s): 71.10.Ca, 73.20.Mf, 73.40.−c

I. INTRODUCTION

In the Fermi liquid theory, the interacting electron system is composed of weakly interacting quasiparticles at low energies with long quasiparticle lifetimes. The effective mass of a quasiparticle, which can be viewed as the bare mass of a free electron being renormalized by electron-electron interactions, is an important and fundamental Fermi liquid parameter. For decades, theorists have been exploring the effective mass renormalization in two- and three-dimensional interacting electron systems (2DES and 3DES). In spite of this great deal of theoretical activity, concentrating almost entirely on the density dependence of the effective mass renormalization, the temperature dependence of the effective mass has not been studied until very recently. Besides the considerable difficulties involved in the finite temperature numerical and analytical many-body calculations in 2DES and 3DES, the reason that this issue has not been addressed before can also be explained by the fact that the Fermi energy in 3D metals is typically 10^4 K, and therefore, any finite-temperature effects are negligible. In the past decade, however, low-density 2DES have been attracting attention, and several experiments have been performed to measure the 2D effective mass.[1,2] The temperature dependence of the quasiparticle effective mass in 2DES is of considerable experimental interest, since the Fermi energy in realistic 2DES may be 1 K or lower, which makes the issue of the temperature dependence of 2D Fermi liquid parameters extremely important. In addition, the temperature dependence of the Fermi liquid parameters, such as the effective mass, is obviously of considerable fundamental theoretical significance.

The $T=0$ quasiparticle effective mass renormalization in an electron system, interacting through long-range Coulomb interaction, is one of the oldest many-body problems in theoretical condensed matter physics, and a number of theoretical calculations of 3D and 2D electron effective mass have been carried out[3–9] in the literature. In fact, Coulomb interaction-induced electron effective mass renormalization at $T=0$ is standard textbook material[7] in electronic many-body theory. Essentially all of these calculations, both analytical and numerical (and both 2D and 3D), are based on the leading-order dynamically screened interaction one-loop self-energy evaluation [the so-called random-phase approximation (RPA) self-energy approximation] because this approximation is really the only meaningful nontrivial calculation that can actually be carried out, and (perhaps more importantly) because this RPA self-energy is asymptotically exact in the weakly interacting high-density regime. There have been a few finite-temperature RPA self-energy calculations over the years,[10–13] mostly in the context of low-dimensional systems, but none for the temperature dependence of the effective mass renormalization in interacting electron systems. Very recently, Chubukov and Maslov[14] considered the problem of temperature corrections to the 2D Fermi liquid theory for the case of a short-ranged interaction. In particular, they showed that the leading many-body temperature correction is linear in two dimensions, similar to the results which we reported recently for the long-range Coulomb interaction in 2DES.[15]

In the current paper, we present a calculation of the density- and temperature-dependent effective mass renormalization by the Coulomb interaction in 2DES and 3DES at arbitrary densities and temperatures (i.e., *not* necessarily restricted to high densities and low temperatures). We work within the RPA, or equivalently in the ring-diagram approximation for the self-energy, which gives exact results in the high-density limit ($r_s \ll 1$), but is known to be qualitatively reliable at relatively low densities as well. RPA is perhaps the only manageable way to perform any nontrivial quantitative calculations in electronic many-body systems, and the finite-temperature RPA effective mass renormalization is certainly a problem of intrinsic interest. In two dimensions, our numerical results predict a nonmonotonic effective mass temperature dependence. The leading temperature dependence is linear and positive, with the low-temperature slope being independent of the electron density in the high-density limit. The temperature at which the effective mass is maximum at a particular density moves toward higher temperatures as density decreases. In three dimensions, we find that the effective mass temperature dependence is nonuniversal and depends on the electron density in a complicated way. At very high densities, the leading correction is positive, while at lower densities it changes sign and decreases monotonically from its zero temperature value. This is in contrast to the 2D results, where the effective mass always increases (linearly) with temperature at low temperatures, and then decreases with temperature beyond a density-dependent characteristic temperature. We find the 3D temperature correction to the effective mass to be nonlinear, in contrast to our 2D results.

We express the quasiparticle effective mass $m^*(n,T) \equiv m^*(r_s, T/T_F)$ in units of the bare band mass m (which is, by definition, a constant) and present our results as a function of the usual dimensional interaction parameter r_s (the average interelectron separation measured in the units of Bohr radius) and the dimensionless temperature T/T_F, where $T_F = E_F/k_B$ is the Fermi temperature. Note that $r_s \propto n^{-1/2}(n^{-1/3})$ in 2D (3D) systems, and $T_F \propto n(n^{2/3})$ in 2D (3D) systems, where n is the appropriate 2D (per unit area) or 3D (per unit volume) electron density. Note that the dimensionless interaction and temperature parameters r_s and T/T_F are *not* independent parameters, since they both depend on the electron density. We also note that $r_s \ll 1$ (high-density) and $r_s \gg 1$ (low-density) limits are, respectively, the weak- and strong-interaction limits of the electron system (at $T=0$), and $T/T_F \ll 1$ and $T/T_F \gg 1$ are, respectively, the low-temperature (quantum) and high-temperature (classical) limits. We consider the electron system to be a uniform jellium system with the noninteracting kinetic energy dispersion being the usual parabolic dispersion. We use $\hbar = k_B = 1$ throughout.

The structure of our paper is as follows: In Sec. II we provide the formalism that we will use in this paper. In Sec. III we explain, in detail, the numerical method we are using in the effective mass calculations. In Sec. IV we present all our numerical results for 2D and 3D effective mass, comparing them to analytical results in the high-density limit. In Sec. V we discuss a special approximation method, the plasmon-pole approximation, and present our effective mass results using this method. In Sec. VI, we calculate the imaginary self-energy of quasiparticles and discuss the validity of the quasiparticle approximation at finite temperatures. We provide a conclusion and discussion of our results in Sec. VII.

II. FORMALISM

In this section we give the theoretical formalism, the basic equations, and the notations that will be used throughout the paper.

A. Effective mass

In a system of interacting fermions, the retarded Green's function can be written as

$$G_R(\mathbf{k},\omega) = \frac{1}{\omega - \varepsilon_0(\mathbf{k}) + \mu - \Sigma(\mathbf{k},\omega)}, \tag{1}$$

where $\varepsilon_0(\mathbf{k}) = k^2/2m$ is the spectrum of noninteracting fermions, μ is the chemical potential, and $\Sigma(\mathbf{k},\omega)$ is the quasiparticle self-energy, the imaginary (real) part of which determines the lifetime (effective mass) of the quasiparticle. The quasiparticle energy can be obtained by solving the Dyson's equation[7]

$$\varepsilon(\mathbf{k}) = \varepsilon_0(\mathbf{k}) + \mathrm{Re}\,\Sigma[\mathbf{k},\varepsilon(\mathbf{k})]. \tag{2}$$

The quasiparticle effective mass can be written by definition as

$$\frac{m^*}{m} = \left[\frac{m}{k}\frac{d}{dk}\varepsilon(\mathbf{k})\,\Big|_{k=k_F}\right]^{-1} = \left.\frac{1 - \dfrac{\partial}{\partial\omega}\mathrm{Re}\,\Sigma(\mathbf{k},\omega)}{1 + \dfrac{m}{k}\dfrac{\partial}{\partial p}\mathrm{Re}\,\Sigma(\mathbf{k},\omega)}\right|_{k=k_F,\omega=0}. \tag{3}$$

Note that in the above equation, $\omega = 0$ is measured from the renormalized chemical potential μ^*, which is given by

$$\mu^* = \mu + \mathrm{Re}\,\Sigma(k_F, 0). \tag{4}$$

All the above equations are exact, while the RPA approximation for $\Sigma(\mathbf{k},\omega)$ that we are going to use is the first- order perturbation theory in the dynamically screened interaction. There has been extensive discussion[3,5,7,16] on whether it is more consistent to use exact Eq. (3) for calculating the effective mass or to use the so-called on-shell approximation, keeping only the first-order interaction terms in the expression for the effective mass (since Σ is calculated only to first order in the dynamically screened interaction):

$$\frac{m^*}{m} = \frac{1}{1 + \left.\dfrac{m}{k}\dfrac{d}{dk}\Sigma(\mathbf{k},\xi_{\mathbf{k}})\right|_{k=k_F}}, \tag{5}$$

where $\xi_{\mathbf{k}} = k^2/(2m) - \mu$. Note that all the quantities on the right-hand side of Eq. (5) are in the leading order in effective interaction. There are compelling arguments in favor of the latter choice: the on-shell approximation is believed to be more accurate as it effectively accounts for some higher-order diagrams and satisfies the Ward identity. We have extensively discussed this issue elsewhere.[16]

Obviously, the two equations for calculating m^* are identical in the high-density limit $r_s \ll 1$. However, in the region of $r_s > 1$, they give very different results. In what follows, we use Eq. (5) for all the numerical results shown in this paper because we believe the on-shell approximation to be the superior one in our case. Both formulas give a similar temperature dependence for $m^*(T)$. The main qualitative results of the paper are insensitive to the choice of the on- or off-shell formula for the effective mass.

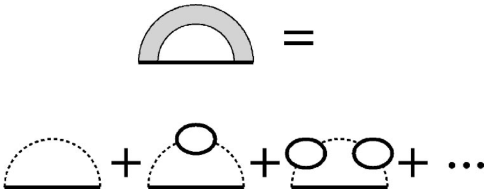

FIG. 1. Feynman diagram for RPA self-energy calculation. Solid lines denote the free electron Green's function and the dashed lines, the bare Coulomb potential.

B. Self-energy in the RPA approximation

Within RPA, the finite temperature electron self-energy can be expressed in terms of the Feynman diagrams shown in Fig. 1, and can be written in the Matsubara formalism as[7]

$$\Sigma(\mathbf{k},\nu_n) = -T\sum_{\omega_m}\mathcal{G}(\mathbf{k}-\mathbf{q},\nu_n-\omega_m)\mathcal{D}(\mathbf{q},\omega_m), \tag{6}$$

where $\nu_n=\pi(2n+1)T$ is the fermion Matsubara frequency, $\omega_m=2\pi mT$ is the boson Matsubara frequency with n and m integers, and T the temperature. The function $\mathcal{D}(\mathbf{q},\omega_m)$ denotes the coupling to a collective mode (phonon, plasmon, electron-hole excitation, etc.), i.e., $\mathcal{D}$ is the bosonic propagator for the effective interaction. In our case, the function is the dynamically screened Coulomb interaction given by the sum of the ring or bubble diagrams:

$$\mathcal{D}(\mathbf{q},\omega_m) = \frac{v_0(\mathbf{q})}{1+v_0(\mathbf{q})\pi(\mathbf{q},\omega_m)}, \tag{7}$$

where $v_0(\mathbf{q})$ is the bare Coulomb interaction and $\pi(\mathbf{q},\omega_m)$ is the (bare) polarization operator, which is defined as

$$\pi(\mathbf{q},\omega_m) = 2\sum_{\nu_n}\int\frac{d^d\mathbf{p}}{(2\pi)^d}\mathcal{G}^{(0)}(\mathbf{p},\nu_n)\cdot\mathcal{G}^{(0)}(\mathbf{p}+\mathbf{q},\nu_n+\omega_m), \tag{8}$$

where d is the dimension of the system and "(0)" denotes the noninteracting system. We mention that Eqs. (7) and (8) together form what is called the RPA for an electron gas, where the bare Coulomb interaction is dynamically screened by the electron dielectric function, which is formed from the infinite series of the polarization bubbles. The corresponding electron self-energy, obtained in the leading-order expansion in the dynamically screened interaction $\mathcal{D}$, is conventionally called the RPA self-energy approximation, although the "dynamical Hartree-Fock" approximation or the "ring-diagram approximation" may be a more appropriate terminology.

For calculations, it is more convenient to use the self-energy defined as a function of the real frequency ω, rather than the Matsubara one. Using the standard procedure of analytic continuation, one obtains the following expression for the analytically continued self-energy:

$$\Sigma^R(\mathbf{k},\omega) = -\int\frac{d^d\mathbf{q}}{(2\pi)^d}\int_{-\infty}^{+\infty}\frac{d\nu}{2\pi}\Bigg[\mathrm{Im}\,G_R^{(0)}(\mathbf{k}-\mathbf{q},\nu+\omega)\times D_R(\mathbf{q},-\nu)\tanh\left(\frac{\nu+\omega}{2T}\right)+G_R^{(0)}(\mathbf{k}-\mathbf{q},\nu+\omega)\times\mathrm{Im}\,D_R(\mathbf{q},\nu)\coth\left(\frac{\nu}{2T}\right)\Bigg], \tag{9}$$

where functions labeled with index "R" are retarded functions, i.e., functions analytical in the upper half-planes of the complex frequency. The corresponding effective interaction can be written as

$$D_R(\mathbf{q},\omega) = \frac{v(\mathbf{q})}{1+v(\mathbf{q})\Pi_R(\mathbf{q},\omega)}, \tag{10}$$

where the retarded polarizability can be obtained from Eq. (8) using the following identities:

$$\Pi_R(\mathbf{q},\omega) = \pi(\mathbf{q},i\omega_n\to\omega+i\eta), \tag{11}$$

where η is a real infinitesimal positive number.

Note that we will almost always use retarded quantities unless otherwise stated. Thus without causing any confusion, we can drop the superscript "R."

C. Effective interaction

The next step toward deriving the renormalization of mass is to obtain expressions for the effective coupling $D(\mathbf{q},\omega)$. We use the long-range bare Coulomb interaction to get

$$v_0^{(2D)}(q) = \frac{2\pi e^2}{q},$$

$$v_0^{(3D)}(q) = \frac{4\pi e^2}{q^2}, \tag{12}$$

and the effective interaction

$$D(\mathbf{q},\omega) = \frac{v_0(\mathbf{q})}{1+v_0(\mathbf{q})\Pi(\mathbf{q},\omega)} = \frac{v_0(\mathbf{q})}{\varepsilon(\mathbf{q},\omega)}, \tag{13}$$

where $\varepsilon(\mathbf{q},\omega)\equiv 1+v_0\Pi$ is the RPA dynamical dielectric function. In the RPA, the full polarizability is approximated by the bare polarizability as in Eq. (8), which is just the bare bubble diagram.

Analytical properties of the propagator Π_0 (where Π_0 denotes the $T=0$ form for the bare polarizability with Π denoting the finite T bare polarizability) are nontrivial even at zero temperature. The zero-temperature polarization for 2DES and 3DES are well known and shown below. For the 2D $T=0$ case, we have

$$\Pi_0{}^{2\mathrm{D}}(q,\omega,\mu) = -\frac{m}{\pi} + \frac{m^2}{\pi q^2}\left[\sqrt{\left(\omega + \frac{q^2}{2m}\right)^2 - \frac{4\mu q^2}{2m}} - \sqrt{\left(\omega - \frac{q^2}{2m}\right)^2 - \frac{4\mu q^2}{2m}}\right], \tag{14}$$

where μ is the chemical potential, the frequency ω can be any complex number, and the branch cut of the square roots are taken so that the imaginary part is positive. For 3D ($T=0$) case we have

$$\Pi_0{}^{3\mathrm{D}}(q,\omega,\mu) = \frac{k_\mu m}{2\pi^2 q^2}\left\{1 + \frac{m^2}{2k_\mu q^3}[4\mu\varepsilon_q - (\varepsilon_q+\omega)^2] \times \ln\left(\frac{\varepsilon_q + qv_\mu + \omega}{\varepsilon_q - qv_\mu + \omega}\right) + \frac{m^2}{2k_\mu q^3} \times [4\mu\varepsilon_q - (\varepsilon_q - \omega)^2] \times \ln\left(\frac{\varepsilon_q + qv_\mu - \omega}{\varepsilon_q - qv_\mu - \omega}\right)\right\}, \tag{15}$$

where $\varepsilon_q = q^2/2m$, μ is the chemical potential and $\mu = k_\mu^2/2m = mv_\mu^2/2$, and the frequency ω can be any complex number.

Finite-temperature polarizability can be easily obtained from those at zero temperature using the following identity:[17]

$$\Pi(q,\omega,\mu;T) = \int_0^\infty d\mu' \frac{\Pi_0(q,\omega,\mu')}{4T\cosh^2\left(\frac{\mu'-\mu}{2T}\right)}. \tag{16}$$

We find Eq. (16) to be the most convenient numerical method for obtaining the finite-T polarizability.

D. Dimensionless parameters

Our 2D and 3D electron system can be characterized by two parameters, namely, density (n) and temperature (T). This immediately leads to two dimensionless parameters r_s and T/T_F characterizing the system, with r_s being the effective zero-temperature interaction strength and T/T_F being the effective temperature (note that they are *not* independent). The definition of r_s is the following: In 2DES, r_s is defined such that

$$\pi r_s^2 a_B^2 n = 1, \tag{17}$$

$$k_F r_s a_B = \sqrt{2}, \tag{18}$$

where n is the 2D electron density, k_F is the Fermi momentum, and $a_B = (me^2)^{-1}$ is the Bohr radius. In 3DES, r_s is defined such that

$$4\pi n a_B^3 r_s^3/3 = 1, \tag{19}$$

$$k_F r_s a_B = (9\pi/4)^{1/3}. \tag{20}$$

The Fermi temperature $T_F \equiv E_F \equiv k_F^2/(2m)$, which goes as $T_F \propto r_s^{-2}$ in both 2D and 3D.

III. NUMERICAL METHODS IN m^* CALCULATIONS IN RPA

In this section we explain in detail our numerical approach for the effective mass calculation within RPA. In carrying out the integrations of self-energy in Eq. (9) in order to obtain the effective mass, we use three different techniques, namely frequency sum, frequency integration, and plasmon-pole approximation (PPA). The first two techniques are equivalent, and we explain them in detail in this section. PPA is a further approximation of RPA, which has been extensively used in the literature.[6,12,18] We discuss the PPA in Sec. V. Since there is no existing literature on the finite-temperature effective mass or self-energy calculation to check our numerical results, it is crucial for us to use these different techniques to ensure the correctness of our numerical calculations. We mention here that our frequency sum results and frequency integration results agree well with each other. The frequency integration result is numerically relatively more noisy and, therefore, in this paper we will only show the frequency sum results. We also check our numerical results against the already known results at $T=0$ and against analytical calculations in the $T/T_F, r_s \to 0$ limit.

A. Frequency integration technique

Equation (9) gives the general formula for the RPA self-energy at real frequencies. It can also be written in a more succinct way as

$$\Sigma(\mathbf{k},\omega) = -\int \frac{d^d q}{(2\pi)^d} v_0(q) n_F(\xi_{\mathbf{q}-\mathbf{k}}) - \int \frac{d^d q}{(2\pi)^d} \int \frac{d\varepsilon}{2\pi} \frac{2v_0(q)\,\mathrm{Im}\,\varepsilon^{-1}(q,\varepsilon)}{\varepsilon + \omega + i\eta - \xi_{\mathbf{q}-\mathbf{k}}} \times [n_F(\xi_{\mathbf{q}-\mathbf{k}}) + n_B(\varepsilon)], \tag{21}$$

where $n_F(x) = 1/[\exp(x/T)+1]$ is the Fermi function and $n_B(x) = 1/[\exp(x/T)-1]$ is the Bose function. This method of calculating the self-energy involves integration over real frequencies, and therefore we call it the frequency integration method. It is also known as the spectral or the Lehmann representation of the self-energy. The derivation of Eq. (21) from Eq. (9) is given in the Appendix.

The self-energy of Eq. (21) is composed of two parts: the exchange part and the correlation part. The (frequency-independent) exchange part is also known as the Hartree-Fock self-energy, and its contribution to the effective mass at $T=0$ is singular in both 2D and 3D. Not surprisingly, this singularity is canceled out by contributions from the correlation part of the self-energy. Effective mass is derived from the self-energy through Eq. (5), and we therefore need to obtain the real part of Eq. (21) by putting $i\eta$ to be 0 and regarding the frequency integration as a principal value integration. It is easy to derive from Eq. (21) that the imaginary part of the self-energy can be written as

$$\operatorname{Im}\Sigma(\mathbf{k},\omega) = -\int \frac{d^dq}{(2\pi)^d} v_0(q) \operatorname{Im}\varepsilon^{-1}(\mathbf{q},\xi_{\mathbf{q}-\mathbf{k}}-\omega) \times [n_B(\xi_{\mathbf{q}-\mathbf{k}}-\omega)+n_F(\xi_{\mathbf{q}-\mathbf{k}})]. \tag{22}$$

The $\operatorname{Im}\Sigma$ is not needed in the effective mass calculation since m^* is a Fermi surface property. But it is important to have some idea of the magnitude of $\operatorname{Im}\Sigma$ in order to ensure that quasi-particles are well defined at finite T.

Numerically carrying out the integration in Eq. (21) is nontrivial: for each momentum $\mathbf{q}$ and frequency ω, a 3D integration is required to obtain $\Sigma(\mathbf{q},\omega)$, and what makes the problem even more difficult is that the $\operatorname{Im}\varepsilon^{-1}(\mathbf{q},\omega)$ term in the integrand is highly nonmonotonic. A careful examination of the dynamical dielectric function tells us that at $T=0$, $\operatorname{Im}\varepsilon^{-1}(\mathbf{q},\omega)$ contains delta functions at plasmon excitation frequencies, and at finite temperatures these delta functions broaden into sharp peaks. Integration over these sharps peaks requires special care. For each $\mathbf{q}$, the position (i.e., frequency) of the sharp peaks can be determined by solving $\operatorname{Re}[\varepsilon(\mathbf{q},\omega)]=0$, and their weight can be determined from $\operatorname{Re}[\varepsilon(\mathbf{q},0)]$ using the Kramers-Krönig relations.

One advantage of the frequency integration method is that in Eq. (21) we can directly put $T=0$ to obtain the zero temperature result, in contrast to the frequency sum method, which we will describe in detail below.

B. Frequency sum technique

Due to the great numerical difficulty in carrying out the frequency integration method introduced above (because it involves integration over highly nonmonotonic or singular functions), it is advisable to seek alternatives. At zero temperature, previous works in calculating self-energy and related quantities often transform the real frequency integration into integrations over imaginary frequencies using the analytic properties of the dielectric function. The purpose of this contour distortion is to avoid singularities along the real axis. At finite temperature, a similar approach can be adopted. At finite temperature, what is different from the zero-temperature case is that we transform the integration into an imaginary frequency summation (or Matsubara frequency summation). Hu and Das Sarma[11] showed in detail, how to perform such a transformation from the real-frequency integration to an imaginary frequency summation. Following the technique of contour distortion introduced in Ref. 11 we can write the RPA self-energy as a sum of the Matsubara frequency along the imaginary axis:

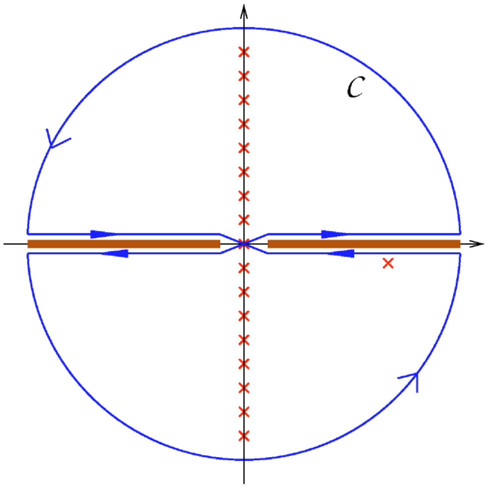

FIG. 2. Contour of integration for the derivation of self-energy formula for the frequency sum method. The thick lines on real axis denotes the branch cut for $\epsilon^{-1}(\mathbf{q},\omega)$. The crosses mark the poles due to the integrand; the ones on the imaginary axis are due to $n_B(\omega)$, and the isolated pole is due to the denominator.

$$\Sigma(\mathbf{k},\omega) = -\int \frac{d^dq}{(2\pi)^d} v_0(q) n_F(\xi_{\mathbf{q}-\mathbf{k}}) - \int \frac{d^dq}{(2\pi)^d} v_0(q) \times \left[\frac{1}{\varepsilon(q,\xi_{\mathbf{q}-\mathbf{k}}-\omega)}-1\right] \times [n_B(\xi_{\mathbf{q}-\mathbf{k}}-\omega)+n_F(\xi_{\mathbf{q}-\mathbf{k}})] - \int \frac{d^dq}{(2\pi)^d} T\sum_{\omega_n} v_0(q) \times \left[\frac{1}{\varepsilon(q,i\omega_n)}-1\right] \times \frac{1}{i\omega_n-(\xi_{\mathbf{q}-\mathbf{k}}-\omega)}, \tag{23}$$

where the frequency sum is over even Matsubara frequencies $i\omega_n = i2n\pi T$, with n integers. The above expression contains three parts, namely the exchange part, the residue part, and the line part from top to bottom in Eq. (23). The proof of the equivalence between Eq. (23) and Eq. (21) is provided below.

Since the exchange part exists in both Eq. (23) and Eq. (21), we only need to consider the correlation part of the self-energy

$$\Sigma^{\mathrm{cor}}(\mathbf{k},\omega) = -\int \frac{d^dq}{(2\pi)^d} \int \frac{d\nu}{2\pi} \frac{2v_0(q)\operatorname{Im}\varepsilon^{-1}(q,\nu)}{\nu+\omega+i\eta-\xi_{\mathbf{q}-\mathbf{k}}} \times [n_F(\xi_{\mathbf{q}-\mathbf{k}})+n_B(\nu)]. \tag{24}$$

We choose the contour as shown in Fig. 2. It is easy to see that the integration over real axis can be transformed into integration over contour C, so that we have

$$\Sigma^{\mathrm{cor}}(\mathbf{k},\omega) = -\int \frac{d^dq}{(2\pi)^d} \oint_C \frac{d\nu}{2\pi i} \frac{v_0(q)[\varepsilon^{-1}(q,\nu)-1]}{\nu+\omega+i\eta-\xi_{\mathbf{q}-\mathbf{k}}} \times [n_F(\xi_{\mathbf{q}-\mathbf{k}})+n_B(\nu)]. \tag{25}$$

This is because $\varepsilon(\mathbf{q},\omega-i\eta)=\varepsilon^*(\mathbf{q},\omega+i\eta)$, and, therefore, the integration of the real part of the integrand right above the real axis in the positive direction and right below the real axis in the negative direction cancel each other, and the corresponding integration of the imaginary part on these two lines are equal to each other. The -1 after $\varepsilon^{-1}(\mathbf{q},\omega)$ is inserted to make the integration on the arc part of contour $\mathcal{C}$ vanishes as the radius of the contour approaches infinity. Now we are left to evaluate the residues within contour $\mathcal{C}$, the positions of which are denoted by crosses in Fig. 2. Note that the analytic property of the dielectric function $\varepsilon^{-1}(\mathbf{q},\omega)$ is very important in this approach. The transformation requires that $\varepsilon^{-1}(\mathbf{q},\omega)$ is analytic in the upper and the lower half of the complex plane, which is true for electron gas systems. The single residue at $\xi_{\mathbf{q}-\mathbf{k}}-\omega-i\eta$, right below the real axis produced by the denominator of the integrand, produces the residue part of the self-energy. This part can be easily derived as

$$\Sigma^{\mathrm{res}} = -\int \frac{d^dq}{(2\pi)^d} v_0(q)\left[\frac{1}{\varepsilon(q,\xi_{\mathbf{q}-\mathbf{k}}-\omega)}-1\right] \times [n_B(\xi_{\mathbf{q}-\mathbf{k}}-\omega)+n_F(\xi_{\mathbf{q}-\mathbf{k}})]. \qquad (26)$$

The residues at $\omega_n=2n\pi T$ on the imaginary axis [the third term in Eq. (23)], which are produced by the Bose function $n_B(\nu)$, lead to the line part of the self-energy. This part can be written as

$$\Sigma^{\mathrm{line}} = -\int \frac{d^dq}{(2\pi)^d} T\sum_{\omega_n} v_0(q)\left[\frac{1}{\varepsilon(q,i\omega_n)}-1\right] \times \frac{1}{i\omega_n-(\xi_{\mathbf{q}-\mathbf{k}}-\omega)}. \qquad (27)$$

From Eq. (26) and Eq. (27) we have $\Sigma^{\mathrm{cor}}=\Sigma^{\mathrm{res}}+\Sigma^{\mathrm{line}}$, and we thus obtain Eq. (23).

The frequency sum method proves to be a far more efficient numerical technique for calculating the self-energy than the frequency integration method due to the absence of the strong nonmonotonicity and singularity in the real frequency dependence of the integrand. One thing to notice is that at high temperatures, higher Matsubara frequency terms can be neglected because $[\varepsilon^{-1}(\mathbf{q},i\omega_n)-1]\rightarrow 0$ when $\omega_n\rightarrow\infty$, while at low temperatures a large number of Matsubara terms have to be kept in the sum in order to ensure accuracy. At zero temperature, the frequency sum turns into an integration over imaginary frequencies, and we have

$$\Sigma(\mathbf{k},\omega) = -\int_{R_1}\frac{d^dq}{(2\pi)^d}v_0(q) + \int_{R_2}\frac{d^dq}{(2\pi)^d}\frac{v_0(q)}{\varepsilon(\mathbf{q},\xi_{\mathbf{q}-\mathbf{k}}-\omega)} - \int\frac{d^dq}{(2\pi)^d}\int\frac{d\nu}{2\pi}\left[\frac{1}{\varepsilon(\mathbf{q},i\nu)}-1\right] \times \frac{\omega-\xi_{\mathbf{q}-\mathbf{k}}}{\nu^2+(\omega-\xi_{\mathbf{q}-\mathbf{k}})^2}, \qquad (28)$$

where the integration region $\mathcal{R}_1$ denotes the region where $|\mathbf{k}-\mathbf{q}|<k$, and $\mathcal{R}_2$ denotes the integration region where $|\mathbf{k}-\mathbf{q}|$ is in between k and k_F. This explicit formula for self-energy is exactly what previous works (see, e.g. Ref. 5) used to calculate the zero-temperature RPA self-energy.

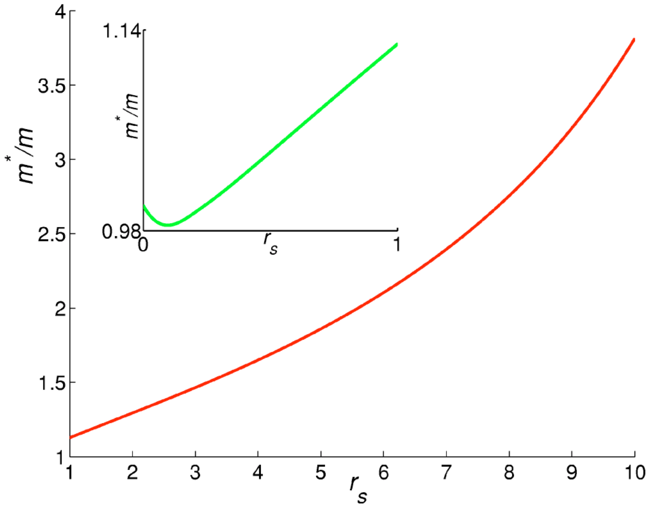

FIG. 3. The calculated $T\sim 0$ effective mass as a function of r_s in a 2DES. Inset: the result in low r_s region.

It is obvious that the frequency-independent exchange part of the self-energy is real. By noticing that $\varepsilon(\mathbf{q},-\omega_n)=\varepsilon^*(\mathbf{q},\omega_n)$, we can see that the line part of the self-energy is real as well. Thus, the only contribution to the imaginary part of the self-energy comes from the residue part, which gives the same result as Eq. (22) in the frequency integration method.

IV. RPA RESULTS FOR $m^*(r_s,T/T_F)$

In this section we present our numerical results for effective mass in 2D and 3D electron systems within RPA. We first present in Sec. IV A results for the zero temperature effective mass to compare with earlier works. Our finite-temperature results for 2DES are presented in Sec. IV B and those for 3DES in Sec. IV C. In Sec. II D we present results for a model bare potential, where the Coulomb interaction is cut off by a finite length so that the bare interaction is short ranged. We do this in order to investigate the model dependence of our results.

A. Zero-temperature effective mass

We first present our extremely low-temperature results ($T/T_F\approx 10^{-4}$) in Figs. 3 and 4, to be compared with the existing $T=0$ results.[3–9] We calculate $m^*(r_s)$ in the $r_s=0-10$ range, showing that the effective mass renormalization could be as large as 4.5 for dilute ($r_s\sim 10$) 2DES and 3 for ($r_s\sim 10$) 3DES. We emphasize that the results presented in Figs. 3 and 4 are entirely based on the $T\rightarrow 0$ limit of our finite temperature theory. They are in *quantitative* agreement with the existing $T=0$ 2D RPA effective mass calculations[5] (which are restricted to the $r_s<5$ regime) and are consistent with the existing $T=0$ 3D effective mass calculations at low r_s.[3] This serves as a stringent check on our numerical approaches.

It is clear from Figs. 3 and 4 that both our 2D and 3D results show the nonmonotonic dependence of $m^*(r_s)$ on r_s in

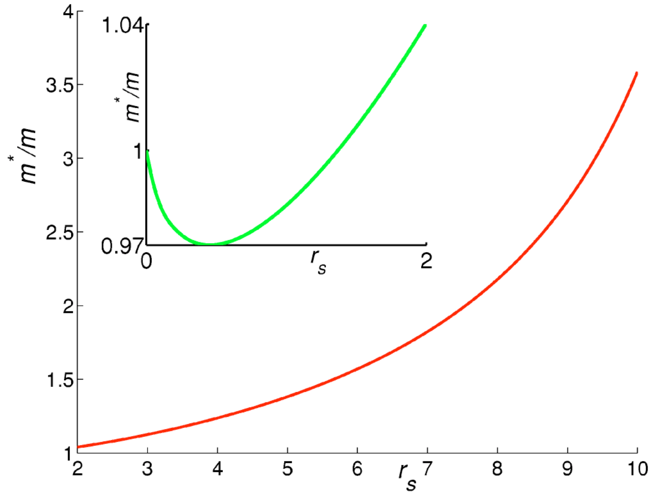

FIG. 4. The calculated $T \sim 0$ effective mass as a function of r_s in a 3DES. Inset: the result in low r_s region.

the high-density regime (i.e., in the $r_s \ll 1$ regime). This nonmonotonic low-r_s behavior for $m^*(r_s)$ at $T=0$ has been reported in the earlier literature.[3,5] We emphasize that the numerical results given in Figs. 3 and 4 are obtained by putting $T/T_F \approx 10^{-4}$ in our finite-temperature formalism.

B. Finite-temperature effective mass in 2DES

In Figs. 5 and 6 we show our calculated 2D $m^*(T)$ as a function of T/T_F for different values of the 2D interaction parameter r_s(=0.1–10). In the low-temperature region, the effective mass first rises to some maximum, and then decreases as temperature increases. This nonmonotonic trend is systematic, and the value of T/T_F where the effective mass reaches the maximum increases with increasing r_s. The initial increase of $m^*(T)$ is almost linear in T/T_F as $T \rightarrow 0$, and the slope $d(m^*/m)/d(T/T_F)$ is almost independent of r_s for very small $r_s(<1)$ (which is shown in Fig. 6), but increases with r_s for larger r_s values. It is important to notice that this nonmonotonic temperature dependence of $m^*(T)$ with a maximum around $T/T_F \lesssim 1$ persists all the way to $r_s \rightarrow 0$, which suggests that it is not an artifact of our approximation scheme, since RPA become *exact* as $r_s \rightarrow 0$. In Sec. VII we will discuss the importance of these features and their agreement with recent analytical works.

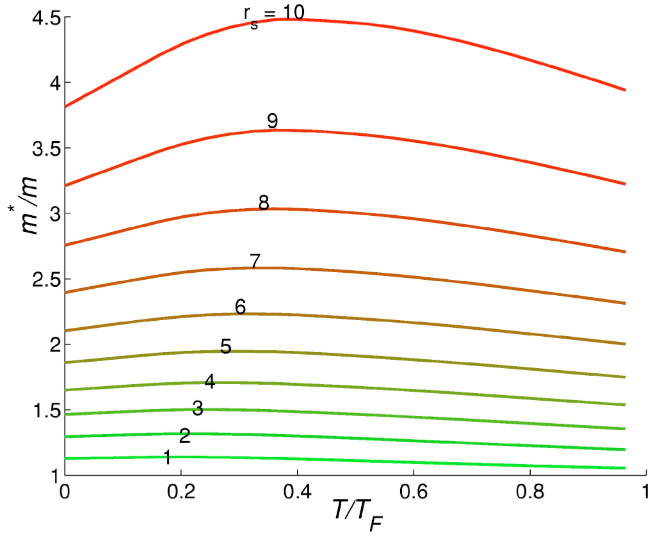

FIG. 5. The calculated 2D effective mass as a function of T/T_F for different r_s: $r_s=10 \rightarrow 1$ from top to bottom. Inset: $r_s=5-1$ from top to bottom. Note that $T_F \propto r_s^{-2}$, making the absolute temperature scale lower for higher r_s values.

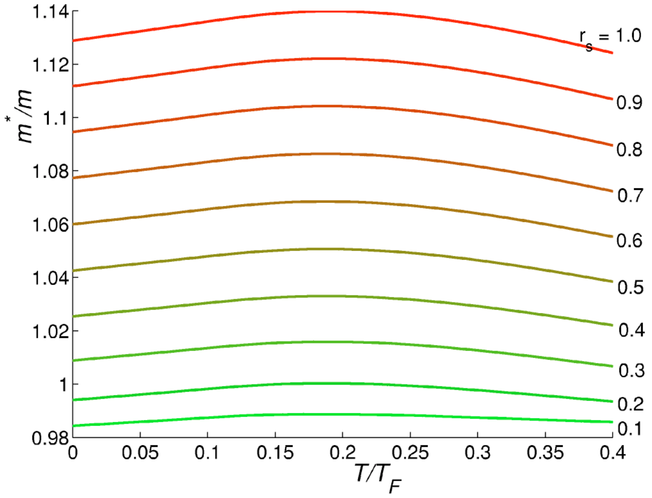

FIG. 6. The calculated 2D effective mass as a function of T/T_F for low r_s values: $r_s=1.0 \rightarrow 0.1$ from top to bottom.

In Figs. 7 and 8 we show the dependence of the effective mass renormalization as a function of the interaction parameter r_s for a few values of fixed temperature (rather than fixed T/T_F, remembering that $T_F \propto r_s^{-2}$ since $T_F \propto n$ and $r_s \propto n^{-1/2}$). Figure 7 shows the effective mass for high T and large r_s values, while Fig. 8 concentrates on the low T region. The calculated $m^*(r_s)$ for fixed T values are quite striking: For low fixed values of T, m^*/m initially increases with r_s even faster than the corresponding $T=0$ result, eventually decreas-

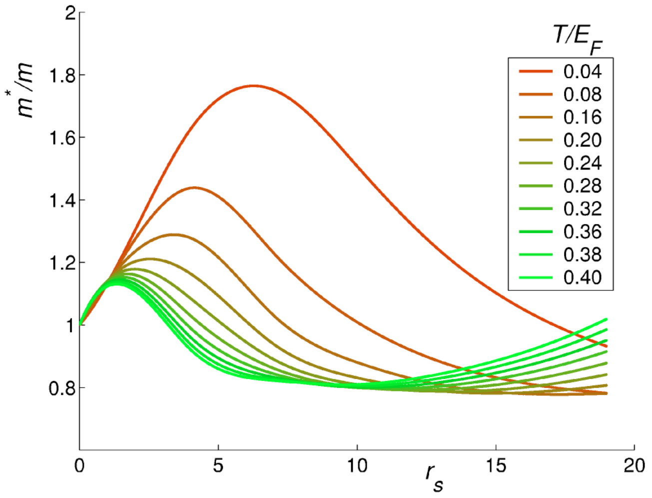

FIG. 7. The calculated 2D effective mass as a function of r_s at fixed value of temperatures. T is in the unit of T_F at $r_s=1$.

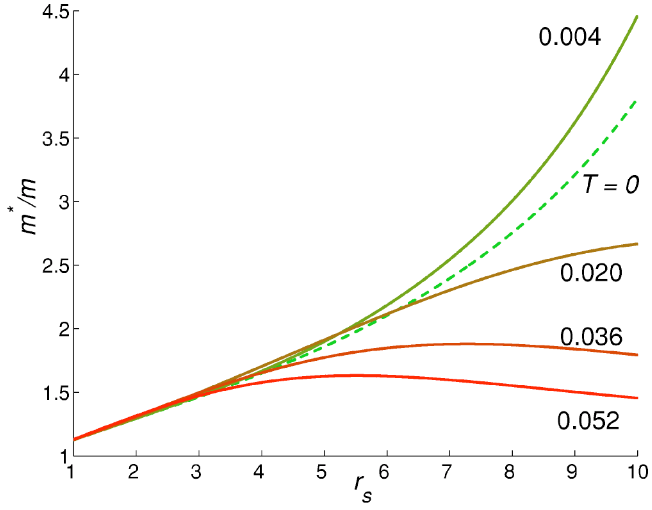

FIG. 8. The calculated 2D effective mass as a function of r_s at fixed value of temperatures. T is in the unit of T_F at $r_s=1$. This plot is similar to Fig. 7, but concentrates on the low-temperature region.

ing with r_s at large enough values (where the corresponding T/T_F values become large enough). This nonmonotonic behavior of $m^*(r_s)$ as a function of r_s for fixed temperatures showing a temperature-dependent maximum (with the value of r_s at which the m^* peak occurs decreasing with increasing T as in Fig. 7) is complementary to the nonmonotonicity of $m^*(T)$ in Fig. 5 as a function of T/T_F (at fixed r_s), and arises from the relationship between the dimensionless variables T/T_F ($\propto r_s^{-2}$) and r_s ($\propto T_F^{-1/2}$) due to their dependence on the carrier density (i.e., $T_F \propto n$ and $r_s \propto n^{-1/2}$). At large r_s and high temperature, Fig. 7 shows that the effective mass increases from below unity with increasing r_s. This is the region where the exchange part of the self-energy dominates, and it can be easily shown that the exchange self-energy produces this peculiar effect on the r_s dependence of $m^*(r_s)$ at fixed high-T values. Since the quasiparticles may not even be well defined at such high T/T_F values, we do not further discuss the physics related to this region.

One immediate consequence of our results shown in Figs. 5 and 7 is that $m^*(T/T_F, r_s) \equiv m^*(T,n)$ in 2DES could show a strong enhancement at low (but finite) temperatures and low electron densities (large r_s). Comparing with the actual system parameters for 2D electrons in Si inversion layers and GaAs heterostructures (and taking into account the quasi-2D form factor effects[19] neglected in our strictly 2D calculation) we find that, consistent with recent experimental findings,[1] our theoretical calculations predict (according to Figs. 5 and 7 as modified by subband form factors) m^*/m to be enhanced by a factor of 2–4 for the experimental densities and temperatures used in recent measurements.[1] Due to the approximate (i.e., RPA) nature of our theory, we do not further pursue the comparison with experimental data in this paper since the main goal of this paper is to discuss the temperature dependence of $m^*(r_s, T/T_F)$ which has not yet been reported in the literature. A direct experimental observation of an increasing $m^*(T)$ at low temperatures in 2DES will be a striking confirmation of our theory.

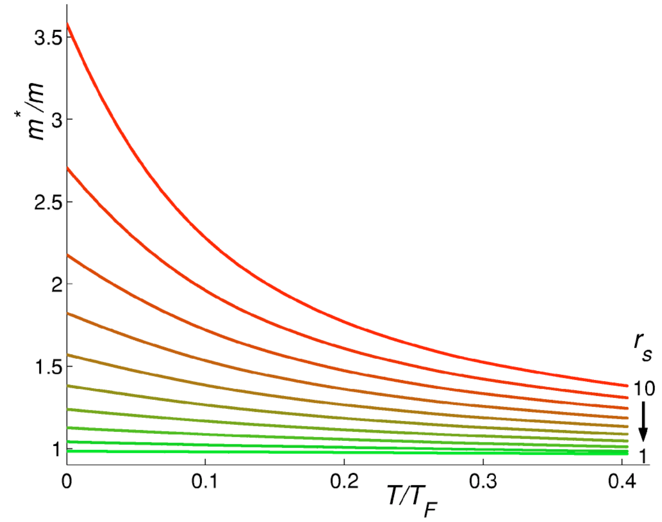

FIG. 9. The calculated 3D effective mass as a function of T/T_F for different r_s: $r_s=10 \rightarrow 1$ from top to bottom.

C. Finite-temperature effective mass in 3DES

In Figs. 9 and 10 we show our calculated 3D $m^*(T)$ as a function of T/T_F for different r_s values. In Fig. 9 r_s varies from 1 to 10, while in Fig. 10, r_s is from 0.1 to 1. The 3D temperature dependence of the effective mass shows very different characteristics from that of 2D. Figure 9 shows that for $r_s > 1$, the effective mass decreases monotonically with increasing T at low temperatures. However for $r_s << 1$, as shown in Fig. 10, the effective mass increases with increasing T in the temperature region we are considering. We therefore conclude that in 3DES the sign of the slope $d(m^*/m)/d(T/T_F)|_{T=0}$ is nonuniversal, which differs from that of 2DES, where the above-mentioned slope is always positive for all r_s. Another interesting feature is that the sign of $d(m^*/m)/d(T/T_F)|_{T=0}$ matches the sign of $-d(m^*/m)/d(r_s)|_{T=0}$ very well. In particular, $m^*(T)$ decreases with increasing T (at low T) in the "larger" r_s regime, where

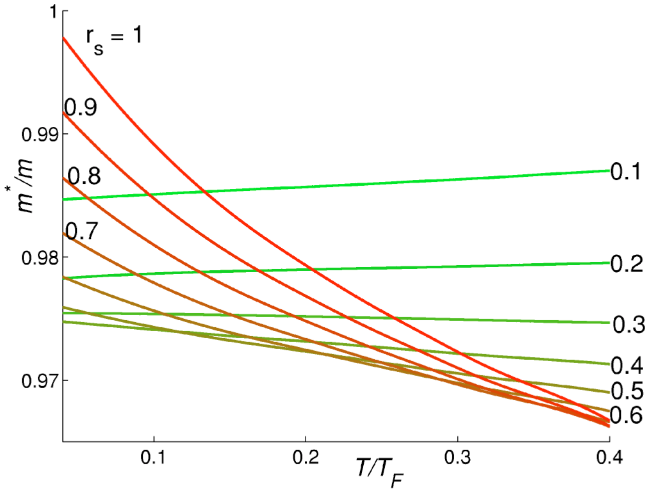

FIG. 10. The calculated 3D effective mass as a function of T/T_F for low r_s values: $r_s=1.0 \rightarrow 0.1$.

the corresponding $T=0$ $m^*(r_s)$ shows an increasing mass with increasing r_s. Similarly, $m^*(T)$ increases (at low T) with increasing T in the r_s regime, where the corresponding $m^*(r_s;T=0)$ shows decreasing m^* with increasing r_s.

D. Model short-range bare interaction

So far, in all of our calculations we have been using the realistic long-ranged Coulomb interaction for the bare potential as in Eq. (12). A question naturally arises: how is the temperature dependence that we find in our calculations related to the long-range nature of the interaction between electrons? Therefore, we also calculate the effective mass in 2DES and 3DES using a simple (parametrized) finite-range interaction model

$$v^{2\mathrm{D}}(q) = \frac{2\pi e^2}{q+a},$$

$$v^{3\mathrm{D}}(q) = \frac{4\pi e^2}{q^2+a^2} \tag{29}$$

where a is the cutoff wave vector that eliminates the long wavelength Coulomb divergence.

Our numerical calculation shows that as $a/k_F \to 0$, we recover the $m^*(T)$ behavior of the bare Coulomb interaction results in both 2D and 3D. As a/k_F increases, the mass renormalization in both 2D and 3D is suppressed, but all the qualitative features of the temperature dependence persist. In 2DES, as a/k_F increases, the temperature where the effective mass reaches the maximum decreases, and the effective mass enhancement (from the $T=0$ value to the maximum) decreases, but the linear-T dependence at low T and the nonmonotonic trend remain unchanged. In 3DES, as a/k_F increases, the r_s region where $d(m^*/m)/d(r_s)|_{T=0} < 0$ shrinks, but the consistency between the sign of $-d(m^*/m)/d(r_s)|_{T=0}$ and the sign of $d(m^*/m)/d(T/T_F)|_{T=0}$ remains.

From these results we conclude that the qualitative features of the temperature dependence are model independent and *not* peculiar to the bare interaction being Coulombic. This conclusion is further reinforced by the recent report of a linearly T-dependent electronic specific heat in a short-range interaction model.[14] It may be worthwhile, however, to note that RPA is specific to the long-range Coulomb interaction in giving an exact result in the high-density $r_s \to 0$ limit, and there is nothing special about RPA in the case of short-range interaction.

V. PLASMON-POLE APPROXIMATION

We now apply a simple-to-use dynamical approximation to calculate $m^*(T)$. The PPA has often been used[6,12,18] to obtain the electron self-energy in the literature. It is a simple technique for carrying out the frequency sum or integration in the RPA self-energy calculation by using a spectral pole (i.e., a delta function) ansatz for the dynamical dielectric function $\varepsilon(\mathbf{k},\omega)$. In other words, it is an approximation to the RPA. The PPA ansatz assumes that

$$-2\,\mathrm{Im}\frac{1}{\varepsilon(\mathbf{k},\omega)} = C_k[\delta(\omega-\overline{\omega}_k) - \delta(\omega+\overline{\omega}_k)], \tag{30}$$

where the pole $\overline{\omega}_k$ and the spectral weight C_k of the PPA propagator in Eq. (30) are determined by using the the Kramers-Krönig relation (i.e., causality)

$$\mathrm{Re}\frac{1}{\varepsilon(k,0)} = 1 + \frac{2}{\pi}\int_0^\infty \frac{1}{\omega} d\omega\, \mathrm{Im}\frac{1}{\varepsilon(k,\omega)} \tag{31}$$

and the f-sum rule (i.e., current conservation)

$$\int_0^\infty \omega\, d\omega\, \mathrm{Im}\frac{1}{\varepsilon(k,\omega)} = -\frac{\pi}{2}\omega_P^2(k). \tag{32}$$

Putting Eq. (30) in Eqs. (31) and (32) we have

$$C_k = \pi\omega_P(k)\sqrt{1-\mathrm{Re}\ \varepsilon^{-1}(k,0)}, \tag{33}$$

$$\overline{\omega}_k = \frac{\omega_P(k)}{\sqrt{1-\mathrm{Re}\ \varepsilon^{-1}(k,0)}}, \tag{34}$$

where $\omega_P(k)$ in Eqs. (32)–(34) is the long-wavelength plasmon frequency, which is defined as

$$\lim_{\omega\to\infty}\mathrm{Re}[\varepsilon(k,\omega)] = 1 - \frac{\omega_P^2(k)}{\omega^2}. \tag{35}$$

It is well known that in 2DES

$$\omega_P^2(k) = \frac{2\pi n e^2}{m}k, \tag{36}$$

and in 3DES

$$\omega_P^2(k) = \frac{4\pi n e^2}{m}. \tag{37}$$

We mention that $\overline{\omega}_k$ in Eq. (30) does not correspond to the real plasmon dispersion in the electron liquid, but simulates the whole excitation spectra of the system behaving as an effective plasmon at low momentum and as the single-particle electron-hole excitation at large momentum, as constrained by the Kramers-Krönig relation and the f-sum rule. Details on the PPA are available in literature,[6,12,18] including its finite-temperature generalization.[12] The PPA, which is known to give results close to the full RPA calculation of self-energy, allows a trivial carrying out of the frequency sum in the retarded self-energy function leading to

$$\begin{aligned}\mathrm{Re}\ \Sigma(\mathbf{k},\omega) = &-\int\frac{d^2q}{(2\pi)^2}v_0(q)n_F(\xi_{\mathbf{q}-\mathbf{k}})\\ &+\int\frac{d^2q}{(2\pi)^2}v_0(q)C_q\Bigg[\frac{n_B(\overline{\omega}_q)+n_F(\xi_{\mathbf{q}-\mathbf{k}})}{\overline{\omega}_q-(\xi_{\mathbf{q}-\mathbf{k}}-\omega)}\\ &+\frac{n_B(-\overline{\omega}_q)+n_F(\xi_{\mathbf{q}-\mathbf{k}})}{\overline{\omega}_q+(\xi_{\mathbf{q}-\mathbf{k}}-\omega)}\Bigg],\end{aligned} \tag{38}$$

where C_q and $\overline{\omega}_k$ only depend on $\varepsilon(k,0)$ at finite temperatures, and are determined by Eqs. (33) and (34). Obviously the PPA provides a great simplification of the problem, since the most numerically demanding part of the calculation (the

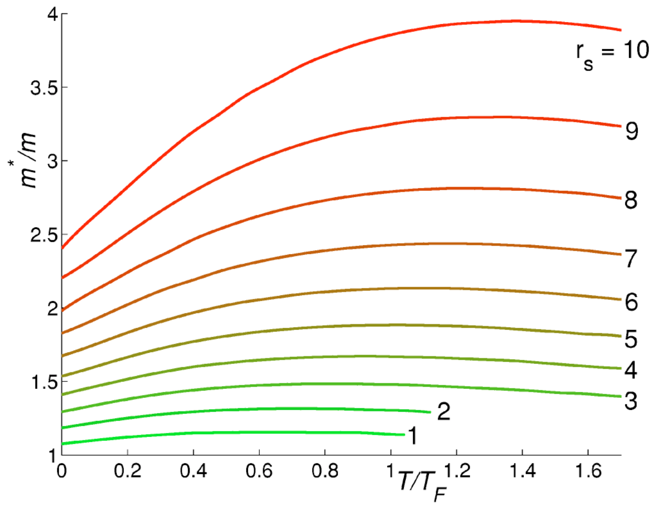

FIG. 11. The calculated 2D PPA effective mass as a function of T/T_F at a fixed value of r_s.

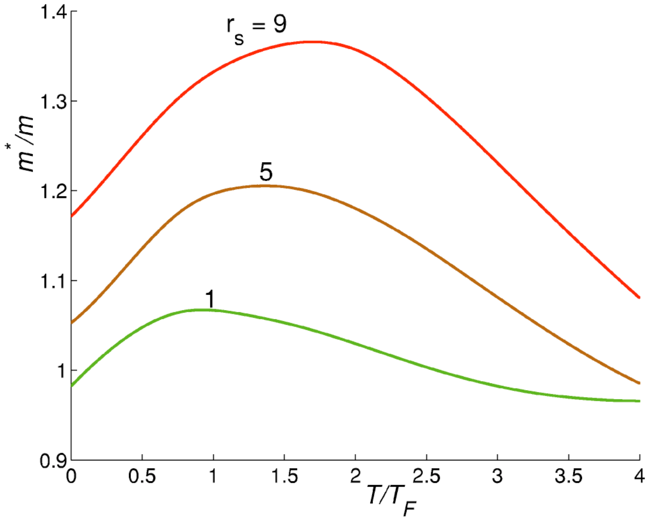

FIG. 12. The calculated 3D PPA effective mass as a function of T/T_F at a fixed value of r_s.

frequency sum or integration) is trivially done. It should be noted, however, that although the PPA is known to produce a reliable approximation to Re Σ, it, by definition, fails completely for Im Σ.

We present our PPA results for the 2D effective mass as a function of T/T_F at fixed r_s values in Fig. 11. One immediate observation by comparing Figs. 5 and 11 is that even though PPA provides a very good approximation for the self-energy (indeed, our numerical results for PPA self-energy and RPA self-energy match very well), it fails to provide accurate results for the effective mass. The zero-temperature effective mass generated by PPA is almost half of that from RPA, and the temperatures where m^* maximizes shift to higher T values in the PPA compared with RPA. But the qualitative behavior of $m^*(r_s,T/T_F)$ is similar in the PPA and RPA for the 2DES as is clear by comparing Figs. 11 and 6.

From our results of 3D PPA effective mass calculation presented in Fig. 12, we can see that they are different from RPA results even qualitatively. In fact, our RPA results for $m^*(r_s,T/T_F)$ are similar in both 2D and 3D.

VI. QUASIPARTICLE DECAY

The quasiparticle decay rate (or the inverse lifetime) is given[10,13] by the imaginary part of the self-energy. As we have discussed in Sec. III B, the imaginary part of the quasiparticle self-energy can be calculated from Eq. (23). It is also obvious that only the second term in Eq. (23) contributes to the imaginary self-energy: the first term is obviously real, and the last term is also real because $\epsilon(\mathbf{q},-\omega_n) = \epsilon^*(\mathbf{q},\omega_n)$. Thus, we have

$$\mathrm{Im}\,\Sigma(\mathbf{k},\omega) = -\int \frac{d^dq}{(2\pi)^d} v_0(q)\,\mathrm{Im}\frac{1}{\epsilon(q,\xi_{\mathbf{q}-\mathbf{k}})} \times [n_B(\xi_{\mathbf{q}-\mathbf{k}}-\omega)+n_F(\xi_{\mathbf{q}-\mathbf{k}})]. \qquad (39)$$

Figures 13 and 14 show the calculated imaginary self-energy on the Fermi surface in 2D and 3D, respectively. The quasiparticle decay (i.e., finite Im Σ) here arises entirely from having a finite temperature. The results show that the magnitude of the imaginary self-energy increases with increasing r_s and T/T_F. It is obvious from Eq. (39) that the imaginary self-energy vanishes on the Fermi surface at $T=0$ as it must, since the quasiparticles are perfectly well defined at $T=0$ for $k=k_F$. As T increases, the magnitude of imaginary self-energy remains small compared to the Fermi energy up to a certain temperature, and the quasiparticles on the Fermi surface remain well defined up to that temperature. The important question is whether the finite-temperature quasiparticles are sufficiently well defined for the interesting behavior of $m^*(T)$ that we discussed in Sec. IV to be experimentally observable. If the quasiparticles are ill defined, (i.e., Im $\Sigma(k_F) > E_F$ in the temperature regime of interest) then obviously all the interesting temperature dependence of $m^*(T)$ predicted by us is only of academic interest since the

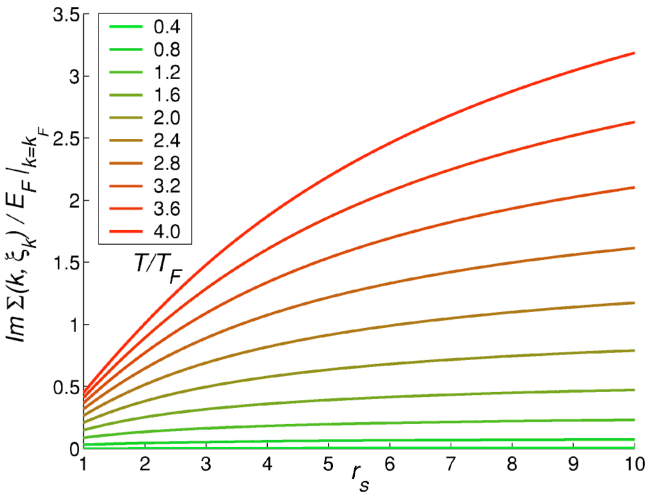

FIG. 13. The calculated magnitude of the 2D RPA imaginary self-energy of quasiparticles on Fermi surface as a function of r_s at different values of T/T_F.

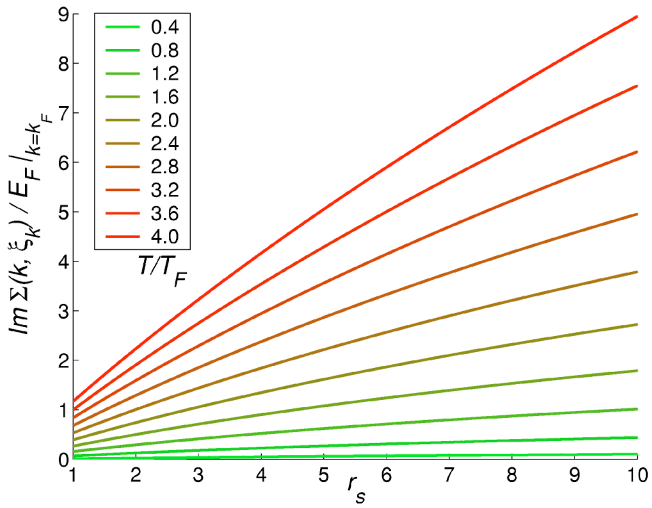

FIG. 14. The calculated 3D RPA imaginary self-energy of quasiparticles on Fermi surface as a function of r_s at different values of T/T_F.

large broadening will make it impossible to define quasiparticles, let alone their effective mass. By examining the results of Figs. 13 and 14 compared with those presented in Sec. IV, it is clear that there is a well-defined regime of $(r_s, T/T_F)$ values where $m^*(T/T_F)$ shows nontrivial temperature dependence with the condition $E_F \gg |\mathrm{Im}\ \Sigma(k_F)|$ well-satisfied so that quasiparticles are well defined. Although this is not unexpected since $|\mathrm{Im}\ \Sigma(T)| \sim T^2$ for $T/T_F \ll 1$, whereas $m^*(T)/m \approx 1 + \mathcal{O}(T)$ in 2D, it is nevertheless important to see that Im Σ remains small in magnitude in the $(r_s, T/T_F)$ regime of interest. Earlier theoretical work on the quasiparticle damping of 2D interacting electron systems can be found in Refs. 8–10 and 13.

VII. DISCUSSION AND CONCLUSION

In this work, we have obtained detailed results for the temperature dependence of the quasiparticle effective mass, $m^*(r_s, T/T_F)$, at arbitrary values of temperature and density in 2D and 3D electron systems interacting via the long-range Coulomb interaction. Our central approximation is the RPA (i.e., the dynamically screened Hatree-Fock self-energy approximation), which is the leading-order one-loop self-energy calculation in a dynamically screened effective interaction expansion. RPA is exact in the high-density $(r_s \to 0)$ limit at $T=0$, and is therefore a controlled nontrivial approximation, which is empirically known to work well for $r_s > 1$ (e.g., metals with $r_s \sim 3-6$ and 2D semiconductors with $r_s \sim 1-10$). We also calculate the finite-temperature imaginary self-energy (i.e., the quasiparticle decay rate or broadening) to ensure that the broadening remains small in the $(r_s, T/T_F)$ parameter regime of our interest, where $m^*(T)$ shows interesting temperature dependence.

As mentioned earlier in the paper, it is well known that at $T=0$, $m^*(r_s)$ can be exactly calculated (in both 2D and 3D) in the asymptotic $r_s \to 0$ limit by systematically expanding the RPA self-energy since ring diagrams (included in the RPA) are the most divergent diagrams in the $r_s \to 0$ limit. Such a zero temperature r_s expansion of RPA gives the following formula for $m^*(r_s)$ in both 2D and 3D:

$$\left.\frac{m^*(r_s)}{m}\right|_{r_s \to 0} = 1 + a r_s(b + \ln r_s) + \mathcal{O}(r_s^2), \tag{40}$$

where a and b are constants of order unity. What we find numerically is that the leading temperature correction to this effective mass formula is linear in T/T_F in 2D and nonlinear in T/T_F in 3D. In this paper, we have calculated $m^*(r_s, T/T_F)$ numerically for the one-loop dynamically screened Hatree-Fock RPA self-energy theory for arbitrary r_s and T/T_F finding nontrivial temperature dependence of the effective mass at all densities.

Our most important result is the unexpected discovery of a strong temperature-dependent quasiparticle effective mass $m^*(T)$ at low temperatures in 2DES. Since the temperature scale for the temperature dependence of $m^*(T)$ is the Fermi temperature, which tends to be high $(\sim 10^4\ \mathrm{K})$ in the 3D electron liquids (i.e., metals), our temperature-dependent effective mass results for 3D systems are mostly of theoretical interest since any actual T dependence of $m^*(T)$ in the $T/T_F 10^{-4}$ regime will be miniscule. Our numerical results for the calculated $m^*(T)$ in 2D systems are consistent with a *linear* leading-order temperature correction for the 2D quasiparticle effective mass: Results in Figs. 5 and 6 can be well fitted to the formula $m^*(T) \approx 1 + A^{2\mathrm{D}}(r_s) + B^{2\mathrm{D}}(r_s)(T/T_F) + \cdots$ for small T/T_F where the slope $B^{2\mathrm{D}}(r_s)$ seems to be a constant independent of r_s (i.e., density) at least in the high-density $(r_s \ll 1)$ limit; for $r_s > 1$ the slope $B^{2\mathrm{D}}(r_s)$ has a weak density dependence increasing somewhat with increasing r_s (but our approximation scheme, RPA, becomes less quantitatively reliable at large r_s, therefore, it is possible that the slope $d(m^*/m)/d(T/T_F)$ is indeed independent of r_s in the $T \to 0$ limit). In addition to this interesting (and unexpected) linear leading-order temperature correction to the quasiparticle effective mass, we also find $B^{2\mathrm{D}}(>0)$ to be positive for all r_s, indicating that in 2DES, the leading-order temperature correction to the effective mass is positive. Thus, $m^*(T)$ increases with increasing T at first, before eventually decreasing as T/T_F increases substantially, leading to a maximum in $m^*(T)$ at some intermediate temperature $T^*(r_s) \sim 0.5T_F$, which is only weakly density dependent (except, of course, through T_F itself). All three of these 2D findings [i.e., linear leading-order T/T_F dependence of m^*, increasing m^* with T/T_F at low temperatures, and the nonmonotonic behavior with a maximum in $m*(T/T_F)$ occurring at $T^* \sim 0.5T_F$] are surprising and unexpected. We are aware of no intuitive physical arguments that can explain these features easily, and, moreover, we do not think such a simple explanation exists, otherwise they will not be claimed as surprising findings. They are intriguing facts unveiled by calculations. In principle, these predictions can be experimentally tested since our calculations presented in Sec. VI show that the quasiparticles remain reasonably well defined (i.e., the broadening, Im Σ, remains small) all the way to T^* and perhaps even above T^*. This is reasonable since the many-body correction to m^* is linear in T/T_F, whereas the broadening

$\mathrm{Im}\,\Sigma \sim (T/T_F)^2$, ensuring that for $T/T_F < 1$, the quasiparticle effective mass is a well-defined quantity. In contrast to the linear (with positive slope) leading-order T dependence we find for all r_s in our calculated 2D $m^*(T)$, our 3D results show nonuniversal $m^*(r_s, T/T_F)$ behavior. In 3D, $m^*(T/T_F)$ increases with increasing T/T_F at low temperatures only for very high densities (small r_s)—for larger r_s values, $m^*(T)$ decreases monotonically with increasing temperature [in sharp contrast to the striking nonmonotonicity in $m^*(T)$ in 2D] and this decrease is more consistent with a nonlinear leading-order temperature dependence (rather than a linear one as in 2D). Our best guess for our numerical results shown in Figs. 9 and 10 is the following equation: $m^*/m \approx 1 + A^{3D}(r_s) + C^{3D}(T/T_F)^l \ln(T_F/T) + \cdots$, where l is a number of the order one (note that numerically fixing the number l is difficult and needs much more work), $C^{3D} > 0$ for $r_s < r_s^*$ and $C^{3D} < 0$ for $r_s > r_s^*$, with r_s^* being approximately the r_s value, where A^{3D} changes from being negative to positive. It is clear that the trends of temperature dependence of effective mass in 2D and 3D are very different, from which we can safely claim that these features are dimensionality dependent. Again, we do not think there exists simple and intuitive explanations for the characteristic difference between 2D and 3D results.

We comment that our numerical results for $m^*(T)$ are consistent with the very recent analytical work[15,20] on the temperature corrections to the effective mass renormalization in 2D and 3D Fermi liquid. The analytical work is necessarily restricted to the $r_s \to 0$ and $T/T_F \to 0$ limit, where the infinite series of ring diagrams to the electron self-energy (depicted in Fig. 1) provides an *exact* leading-order asymptotic answer to the problem with the following result:

$$\frac{m^*(r_s, T/T_F)}{m} = 1 + A(r_s) + B(r_s)\left(\frac{T}{T_F}\right) + C(r_s)\left(\frac{T}{T_F}\right)^2 \ln\left(\frac{T}{T_F}\right) + \cdots, \tag{41}$$

with $B(r_s) \equiv B^{2D}$, a constant, in 2D, and $B(r_s) \equiv 0$ in 3D. Our numerical results are consistent with this exact result, but our numerical results apply also in the nonasymptotic region, where T/T_F and r_s are not necessarily small. In this nonasymptotic regime (where r_s is *not* small, and actually r_s may be large in 2D semiconductor systems) RPA is by no means an exact theory, but we have recently argued[16] that RPA remains qualitatively well valid, even for $r_s \gg 1$. We also emphasize a point in this context that seems not to have been widely appreciated in the literature. The point is that RPA becomes a progressively better approximation as T/T_F increases at a fixed r_s (for any r_s), because the system is becoming more classical in the $T/T_F \gg 1$ regime. In the classical limit, leaving out three-body and higher-order terms, the only effect of interaction is to dynamically screen the long-range Coulomb interaction, which is exactly incorporated in RPA. Thus, RPA should work better since it correctly incorporates the self-consistent screening of Coulomb interaction (i.e., the dynamical Hartree effect), which should be the most important effect in the classical limit in a Coulomb plasma. In plasma physics, all one needs is to screen the Coulomb interaction. Thus, in the $(r_s, T/T_F)$ parameter space (see Fig. 15), RPA works extremely well as $r_s \to 0$ (the high-density limit) and as $T_F \to 0$ (the high-temperature or equivalently, the low-density limit) or, as $T \to \infty$. As a result, the regime of validity of RPA is greatly enhanced at finite temperature, and in fact even at very large r_s (i.e., very low density) RPA works better as T is raised (because the $T/T_F \gg 1$ limit is more easily achieved at low densities). On the other hand, we want to emphasize that in the extreme high T/T_F limit, we do not seek comparison between our numerical result, as shown in Fig. 7, and the experimental results, because at such high temperature, the physics in a real system becomes much more complicated, and the quasiparticles may not even be well defined.

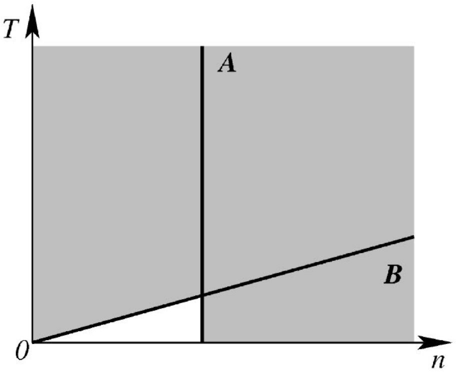

FIG. 15. The schematic validity of RPA. The shaded area denotes the region where RPA is considered to be valid. Line A denotes a certain density value above which RPA is valid at $T=0$ (e.g., the vertical line A may correspond to the $r_s=1$ condition so that for higher density, i.e., to the right of line A, RPA is valid even at $T=0$). Line B denotes the line of $T_F \propto n$. In the region above line B, RPA is again valid. Therefore, for any fixed value of density n (or equivalently fixed r_s), RPA is a better approximation with increasing T, whereas for a fixed value of temperature, low density values (or large r_s) counterintuitively make RPA valid again since RPA is valid for $T > T_F$.

Finally, we comment on the anomalous (often referred to as "nonanalytic")[14] nature of the temperature corrections to the quasiparticle effective mass in 2D systems (but *not* in 3D) as manifested in the *linear* leading-order temperature correction we find in interacting 2D electron systems. This particular feature is apparently generic in 2D and not due merely to our using the long-range bare Coulomb interaction, because in Ref. 14 the same linear-T correction is found in calculations using a zero-range bare interaction, although the sign of the slope is negative in the zero-range interaction case. This kind of (leading-order) linear temperature correction is quite common in 2D electron systems due to the peculiar form of the 2D polarizability with a $T=0$ cusp at $2k_F$. This leading-order linear-T correction is interesting because the naive expectation in a Fermi system (based on the usual Sommerfeld expansion of the Fermi functions) is that the leading-order correction in a "normal" situation should always be $\mathcal{O}(T/T_F)^2$ for all electronic properties. In 2D electron systems it seems that the generic situation is "anomalous," i.e., the leading-order temperature correction is $\mathcal{O}(T/T_F)$ rather than the "normal" quadratic Fermi behavior expected on the basis of the analytic Sommerfeld expansion of Fermi functions. In 2D interacting electron systems, therefore, all leading-order thermal corrections to electronic properties are much stronger (by a factor of T_F/T, which is a large number as $T\to 0$) than the quadratic Fermi gas behavior. This anomalous nonanalyticity, which may have important consequences for fermionic quantum critical phenomena, obviously has important experimental implications, since it is much easier to observe a linear temperature correction than a quadratic one at low temperatures.

ACKNOWLEDGMENTS

This work is supported by the US-ONR, the NSF, and the LPS.

APPENDIX

Here, we provide a proof for equivalence between Eq. (23) and Eq. (21).

$$\begin{aligned}\Sigma(\mathbf{k},\omega) &= -\int \frac{d^dq}{(2\pi)^d}\int\frac{d\nu}{2\pi}\left\{\text{Im } G_R(\mathbf{k}-\mathbf{q},\nu+\omega)D_R(\mathbf{q},\nu)\tanh\left(\frac{\nu+\omega}{2T}\right) + G_R(\mathbf{k}-\mathbf{q},\nu+\omega)\text{Im } D_R(\mathbf{q},\nu)\coth\left(\frac{\nu}{2T}\right)\right\}\\ &= -\int \frac{d^dq}{(2\pi)^d}\int\frac{d\nu}{2\pi}v_0(q)\left\{-\pi\delta(\nu+\omega-\xi_{\mathbf{q}-\mathbf{k}})\epsilon^{-1}(\mathbf{q},\nu)\tanh\left(\frac{\nu+\omega}{2T}\right)+\frac{1}{\nu+\omega+i\eta-\xi_{\mathbf{q}-\mathbf{k}}}\text{Im } \epsilon^{-1}(\mathbf{q},\nu)\coth\left(\frac{\nu}{2T}\right)\right\}.\end{aligned} \tag{A1}$$

Using Kramers-Krönig relations for $\epsilon^{-1}(q,\nu)$ in the above equation, we have

$$\begin{aligned}\Sigma(\mathbf{k},\omega) &= -\int \frac{d^dq}{(2\pi)^d}\int\frac{d\nu}{2\pi}v_0(q)\left\{-\pi\delta(\nu+\omega-\xi_{\mathbf{q}-\mathbf{k}})\times\left[1+\int\frac{d\nu'}{\pi}\frac{\text{Im } \epsilon^{-1}(q,\nu')}{\nu'-\nu-i\eta}\right]\tanh\left(\frac{\nu'+\omega}{2T}\right)\right.\\ &\quad\left.+\frac{1}{\nu+\omega+i\eta-\xi_{\mathbf{q}-\mathbf{k}}}\text{Im } \epsilon^{-1}(\mathbf{q},\nu)\coth\left(\frac{\nu}{2T}\right)\right\}\\ &= -\int\frac{d^dq}{(2\pi)^d}v_0(q)\left\{-\frac{1}{2}\left[1+\int\frac{d\nu}{\pi}\frac{\text{Im } \epsilon^{-1}(q,\nu)}{\nu+\omega+i\eta-\xi_{\mathbf{q}-\mathbf{k}}}\right]\tanh\left(\frac{\xi_{\mathbf{q}-\mathbf{k}}}{2T}\right)+\int\frac{d\nu}{2\pi}\frac{1}{\nu+\omega+i\eta-\xi_{\mathbf{q}-\mathbf{k}}}\text{Im } \epsilon^{-1}(\mathbf{q},\nu)\coth\left(\frac{\nu}{2T}\right)\right\}\\ &= \int\frac{d^dq}{(2\pi)^d}v_0(q)\frac{1}{2}\tanh\left(\frac{\xi_{\mathbf{q}-\mathbf{k}}}{2T}\right)+\int\frac{d^dq}{(2\pi)^d}\int\frac{d\nu}{2\pi}\frac{v_0(q)\text{Im } \epsilon^{-1}(q,\nu)}{\nu+\omega+i\eta-\xi_{\mathbf{q}-\mathbf{k}}}\times\left[\tanh\left(\frac{\xi_{\mathbf{q}-\mathbf{k}}}{2T}\right)-\coth\left(\frac{\nu}{2T}\right)\right]\\ &= \text{const}-\int\frac{d^dq}{(2\pi)^d}v_0(q)n_F(\xi_{\mathbf{q}-\mathbf{k}})-\int\frac{d^dq}{(2\pi)^d}\int\frac{d\nu}{2\pi}\frac{2v_0(q)\text{Im } \epsilon^{-1}(q,\nu)}{\nu+\omega+i\eta-\xi_{\mathbf{q}-\mathbf{k}}}\times[n_F(\xi_{\mathbf{q}-\mathbf{k}})+n_B(\nu)].\end{aligned} \tag{A2}$$

---

[1] V. M. Pudalov, M. E. Gershenson, H. Kojima, N. Butch, E. M. Dizhur, G. Brunthaler, A. Prinz, and G. Bauer, Phys. Rev. Lett. **88**, 196404 (2002); A. A. Shashkin, S. V. Kravchenko, V. T. Dolgopolov, and T. M. Klapwijk, Phys. Rev. B **66**, 073303 (2002); A. A. Shashkin, M. Rahimi, S. Anissimova, S. V. Kravchenko, V. T. Dolgopolov, and T. M. Klapwijk, Phys. Rev. Lett. **91**, 046403 (2003).

[2] J. L. Smith and P. J. Stiles, Phys. Rev. Lett. **29**, 102 (1972); P. T. Coleridge, M. Hayne, P. Zawadzki, and A. S. Sachrajda, Surf. Sci. **361–361**, 560 (1996); W. Pan, D. C. Tsui, and B. L. Draper, Phys. Rev. B **59**, 10208 (1999).

[3] T. M. Rice, Ann. Phys. (N.Y.) **31**, 100 (1965).

[4] M. Gell-Mann, Phys. Rev. **106**, 369 (1957).

[5] C. S. Ting, T. K. Lee, and J. J. Quinn, Phys. Rev. Lett. **34**, 870 (1975).

[6] B. Vinter, Phys. Rev. Lett. **35**, 1044 (1975).

[7] A. A. Abrikosov, L. P. Gor'kov, and I. E. Dzyaloshinski, *Methods of Quantum Field Theory in Statistical Physics* (Dover, New York, 1963); G. D. Mahan, *Many-Particle Physics* (Plenum, New York, 1981); A. L. Fetter and J. D. Walecka, *Quantum Theory of Many-particle Systems* (McGraw-Hill, San Francisco, 1971).

[8] R. Jalabert and S. Das Sarma, Phys. Rev. B **40**, 9723 (1989).

[9] I. K. Marmorkos and S. Das Sarma, Phys. Rev. B **44**, 3451 (1991).

[10] A. V. Chaplik, Sov. Phys. JETP **33**, 997 (1971).

[11] B. Y. K. Hu, Phys. Rev. B **47**, 1687 (1993); B. Y. K. Hu and S. Das. Sarma, *ibid.* **48**, 5469 (1993).

[12] S. Das Sarma, P. K. Kalia, M. Nakayama, and J. J. Quinn, Phys. Rev. B **19**, 6397 (1979); S. Das Sarma and B. Vinter, *ibid.* **28**, 3639 (1983).

[13] G. F. Giuliani and J. J. Quinn, Phys. Rev. B **26**, 4421 (1982); L. Zheng and S. Das Sarma, *ibid.* **53**, 9964 (1996).

[14] A. V. Chubukov and D. L. Maslov, cond-mat/0304381; Phys. Rev. B **68**, 155113 (2003) .

[15] S. Das Sarma, V. M. Galitski, and Y. Zhang, cond-mat/0311559; Phys. Rev. B (to be published).

[16] Y. Zhang and S. Das Sarma, cond-mat/0312565.

[17] P. F. Maldague, Surf. Sci. **73**, 296 (1978).

[18] B. I. Lundqvist, Phys. Kondens. Mater. **6**, 206 (1967); A. W. Overhauser, Phys. Rev. B **18** 2884 (1978).

[19] T. Ando, A. B. Fowler, and F. Stern, Rev. Mod. Phys. **54**, 437 (1982).

[20] S. Das Sarma, V. M. Galitski, and Y. Zhang, Phys. Rev. B **69**, 125334 (2004) .